WILEY | Hindawi

Research Article

Injection Rate-Dependent Deflecting Propagation Rule of Hydraulic Fracture: Insights from the Rate-Dependent Fracture Process Zone of Mixed-Mode (I-II) Fracturing

Yuekun Xing (iD) **and Bingxiang Huang** (iD)

State Key Laboratory of Coal Resources and Safe Mining, China University of Mining and Technology, Xuzhou 221116, China

Correspondence should be addressed to Bingxiang Huang; huangbingxiang@cumt.edu.cn

Mixed-mode (I-II) fracturing is a prominent mechanical characteristic of hydraulic fracture (HF) deflecting propagation. At present, understanding the effect of injection rates on HF deflecting propagation remains challenging and restricts the control of HF deflecting propagation bearing tensile and shear stresses with fluid injection rates. Our recently published experimental results show that the fracture process zone (FPZ) length of mixed-mode (I-II) fractures in rock-like materials increases with the rising quasistatic loading rate. Both the deformation in FPZ and the generation of real fracture surfaces are tensile. On this basis, the rate-dependent mixed-mode (I-II) cohesive fracture model was proposed under quasistatic loading, and a couple of theoretical outcomes were obtained. Under different injection rates, the deflecting HF propagates step-by-step under mixed-mode (I-II) fracturing, and the HF extension path is supposed to be straight in each step. With the increment of injection rate, the increased (tensile) FPZ length is the stable propagation distance of deflecting HF in each step and besides deteriorates the fracture resistance discontinuity of FPZ developing to be a real tensile fracture. Thus, the mixed-mode (I-II) fracture tends to propagate unstably driven by kinetic energy once FPZ develops completely under fast loading. Moreover, two injection rate-dependent (IRD) HF deflecting propagation modes were determined, i.e., the step-by-step stable-propagation and step-by-step unstable propagation modes. HF deflection occurs in the step alternation of fracture propagation. With the increasing fluid injection rate, the increased FPZ length and kinetic energy (from fracture resistance discontinuity) extend the stable and unstable HF propagation distance along the initial direction in an extension step, respectively. Therefore, fast fluid injection improves the HF deflecting propagation radius; i.e., it inhibits the HF deflecting propagation or promotes HF extension along the initially designed direction. The injection rate-dependent HF deflecting propagation modes (based on the proposed model) were validated by further processing of published true triaxial physical simulation tests of hydraulic fracturing. The ordinal response of Fiber Bragg grating sensors embedded along the fracture propagation path, and the continuous fluctuant injecting pressures validate the step-by-step propagation of the hydraulic fracture. The test-measured deflecting HF trajectory indicates that high fluid injection rates remarkably increase the HF deflecting radius, which is consistent with the theoretical analysis in this work. The above findings can provide theoretical bases for controlling the HF deflecting propagation in the surrounding rock of mines and oil-gas reservoirs.

1. Introduction

In the mine, weakening the hard roof above the coal seam by hydraulic fracturing is a significant technical means to prevent the sudden collapse of the hard roof, avoiding dynamic disasters [1, 2]. For oil/gas exploitation, directional perforation hydraulic fracturing is a practical approach to improve the permeability and oil drainage area of the oil-gas reservoirs [3, 4]. Due to disturbance stresses caused by excavation in the mine and the directional perforating in oil/gas reservoirs, the designed HF extension direction is always oblique to the principal directions of in situ stresses. Consequently, HF propagates along a deflecting trajectory and presents shape-s (Figure 1). Due to in situ stresses and net pressure
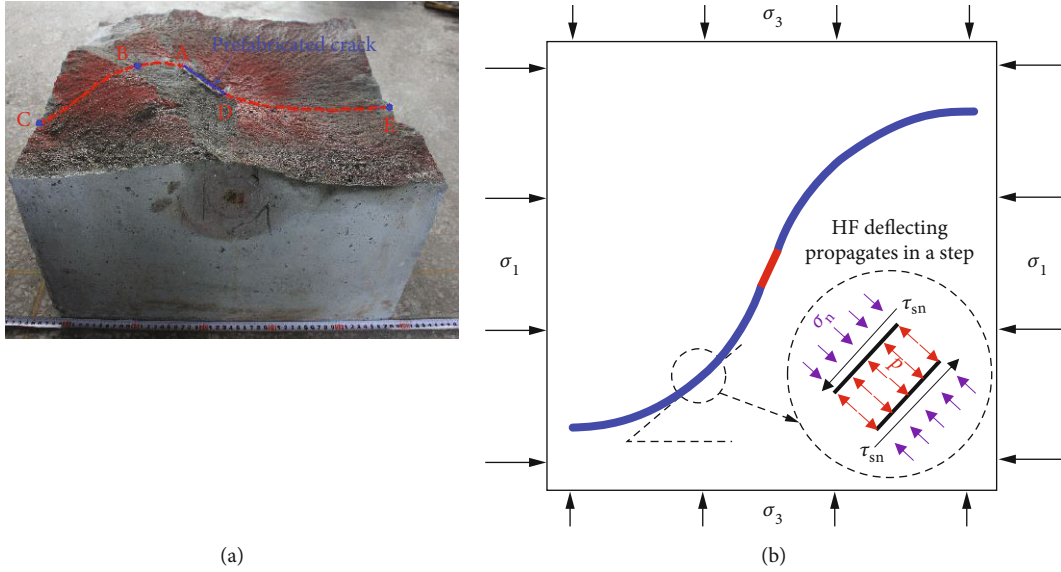
FIGURE 1: The photo and diagram of the deflecting hydraulic fracture: (a) photos of the HF deflecting propagation with hydraulic fracturing physical simulation tests (our previous work); (b) the diagram of deflecting HF bearing tensile and shear stresses.

of the hydraulic fluid, the deflecting HF (Figure 1(a)) bears the tensile-shear combined stresses and follows mixed-mode (I-II) fracturing [3] (Figure 1(b)). Therefore, controlling the HF deflecting propagation under mixed-mode (I-II) fracturing conditions is fundamental to enhancing the hard roof weakening in the mine and improving permeabilities in oil-gas reservoirs. Since the fluid injection rate is a significant parameter for controlling HF propagation, the injection rate-dependent deflecting propagation rule of the hydraulic fracture is the theoretical basis for controlling HF in field applications.

To date, investigations of the HF deflecting propagation rules focus on the effects of horizontal in situ stresses differences, fracture initiation azimuth, and disturbance stress on HF deflecting trajectory [3–6]. However, researches on injection rate-dependent (IRD) HF deflecting propagation are relatively limited [7, 8]. The limited studies, conducted by true triaxial physical simulation tests of hydraulic fracturing [8] and extended finite element (XFEM) simulations [7], reveal that the increased injection rates remarkably extend the HF deflecting distance. The above investigation provides references for the effective control of HF deflecting propagation. However, the HF deflecting propagation model was not proposed based on the above hydraulic fracturing experiments; besides, the fracture model employed in the above XFEM simulations is independent of fluid injection rates. Therefore, theoretical characterization of the rate-dependent mixed-mode (I-II) fracturing in rock-like materials is fundamental to revealing the IRD HF deflecting rule.

Mixed-mode (I-II) fracturing is a prominent mechanical characteristic of HF deflecting propagation. As of now, elastic mixed-mode (I-II) fracture models, such as the maximum stress criterion [9], the maximum energy release rate criterion [10], the minimum strain energy density criterion [11], and other modified models [12] of above criteria, were most widely used to characterizing fracture initiation directions.

However, the above mixed-mode (I-II) fracture models are independent of loading rates. Rate-dependent fracturing characteristics of rock-like materials were mainly investigated with fracturing experiments, focus on mode I (tensile) fractures, whereas researches on mixed-mode (I-II) fractures are relatively limited. Most experimental results show both the mode I (tensile) and mixed-mode (I-II) cracks of rock-like materials, such as concrete [13], shale [14], granite [15], and marble [16, 17], have similar rate-dependent fracture behaviors. More specifically, the elastic fracture resistances (fracture toughness or energy release rate) are strengthened with loading rates increasing. The enhanced fracture resistance is attributed to the insufficient development of plastic strains and intergranular cracks under fast loading [13–15, 18]. The above investigations significantly deepen the understanding of the rate-dependent fracture behavior during HF deflecting propagation. Nevertheless, previous investigations still have two limitations. (1) The previous investigations mainly reveal the rate-dependent elastic fracturing characteristics of mixed-mode (I-II) crack in rock-like materials, neglecting the rate-dependent development of fracture process zone (FPZ). Note that FPZ is a nonnegligible microcrack zone ahead of the mixed-mode (I-II) fracture tip, which is the prominent fracture characteristic of rock-like materials [19–23]. Hence, the traditional fracture model cannot delineate the rate-dependent FPZ growth in HF deflecting propagation. (2) The classic elastic mixed-mode fracture model mainly describes the rate-independent elastic fracture initiation and is not well-suited for HF deflecting propagation with FPZ remarkable development [24–27]. Therefore, characterizations of IRD HF deflecting propagation lack the applicable mixed-mode (I-II) fracture model for rock-like materials.

Given that the fluid injection of hydraulic fracturing is usually quasistatic, in our recently published work [28], the quasistatic rate-dependent FPZ development of mixed-
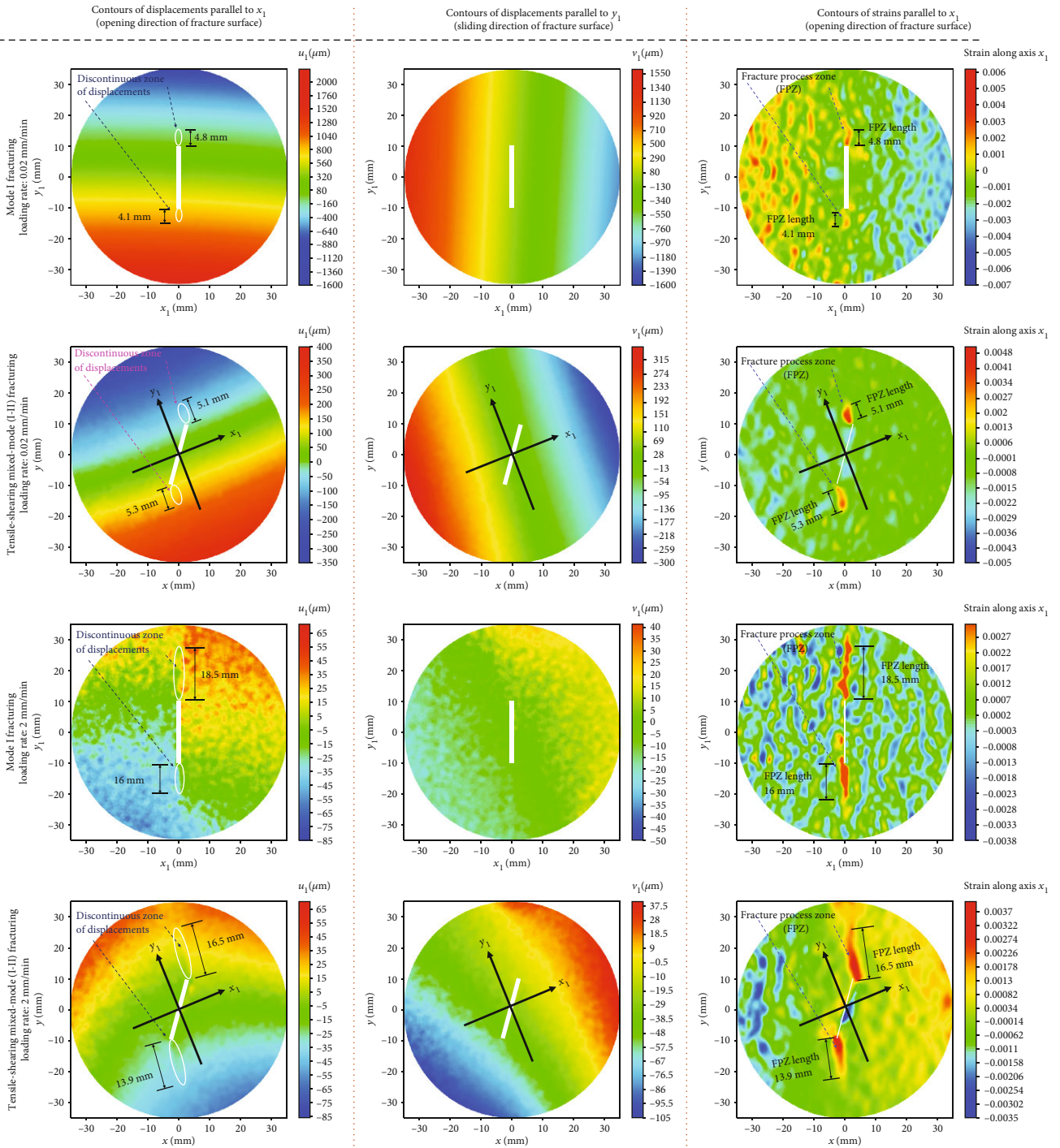
FIGURE 2: DIC-based displacement and strain fields of Mixed-mode (I-II) and pure mode I fracturing at different quasistatic loading rates (replotted based on our recently published work [28]).

mode (I-II) fracturing has been investigated. In detail, we conducted the mixed-mode (I-II) fracturing tests on the centrally cracked Brazilian disk (CCBD) specimens (radius: 50 mm) of artificial rock-like materials to create tensile-shearing mixed-mode (I-II) fractures at different quasistatic displacement loading rates (0.02~2 mm/min). The FPZ development ahead of the mixed-mode fracture tip was characterized with the digital image correlation (DIC) method.

Two main findings were obtained. (1) At different loading rates, in the FPZ ahead of mixed-mode (I-II) fracture tips, the opening displacement perpendicular to the FPZ development direction presents a remarkable discontinuity; in contrast, the sliding displacement parallel to FPZ development direction is continuous (Figure 2). This mixed-mode (I-II) fracturing feature is consistent with the pure mode I fracturing, as shown in Figure 2. Consequently, at different

quasistatic loading rates, the tensile-shearing mixed-mode (I-II) fracturing just represents the fracture bearing tensile-shearing stresses for rock-like materials. Still, at the mixed-mode (I-II) fracture tip, the deformation in FPZ and the generation of the real fracture surface are tensile. (2) The FPZ length and the peak load increase with the rising loading rate (Figure 3) from 0.02 mm/min to 2 mm/min. Note that the increment of FPZ length (Figure 3(b); FPZ length increased by 287%) is much more remarkable than the peak load (Figure 3(a); FPZ increased by 66%). These rate-dependent mixed-mode fracturing characteristics provide significant bases for the theoretical understanding of the injection rate-dependent HF deflecting propagation rule.

In this work, we proposed a rate-dependent mixed-mode (I-II) fracturing model, with insights from the rate-dependent FPZ of mixed-mode (I-II) fracturing (our recently published work [28]). Based on the rate-dependent mixed-mode (I-II) fracture model, we obtained several theoretical outcomes of the injection rate-dependent HF propagation rule, which was validated with the physical simulation tests of HF deflecting propagation.

2. Model Bases of the Injection Rate-Dependent HF Deflecting Propagation

Mixed-mode (I-II) fracturing is a prominent mechanical behavior of HF deflecting propagation. In this section, we will propose a rate-dependent mixed-mode (I-II) fracturing model, with insights from the rate-dependent FPZ of mixed-mode (I-II) fracturing [28], delineating the experiment-measured tensile fracturing characteristic of the mixed-mode (I-II) fracture in rock-like materials. Then, the rate-dependent fracture initiation and deflecting propagation will be theoretically analyzed with the correlation between the fracture driving force and resistance (i.e., the fracture resistance curve). These theoretical investigations are fundamental to revealing the correlation between HF deflecting propagation behavior and fluid injection rates.

2.1. Rate-Dependent Mixed-Mode (I-II) Cohesive Crack Model of the FPZ Development. As mentioned in Section 1, the FPZ deformation ahead of the mixed-mode (I-II) fracture tip has been validated to be tensile, and FPZ length is increased with the rising loading rate (Figures 2 and 3). Therefore, the tensile-shearing mixed-mode (I-II) fracturing in rock-like materials just represents the fracture bearing mixed-mode tensile and shear stresses. Still, at the mixed-mode (I-II) fracture tip, both the deformation in FPZ and the generation of the real fracture surface are tensile. Based on this, the rate-dependent tensile fracturing model and the further theoretical analyses of the mixed-mode (I-II) fracture will be proposed in this section, following three assumptions as below:

(1) The tensile FPZ ahead of the mixed-mode (I-II) fracture can be regarded as a tensile cohesive crack [20–22, 29, 30]

(2) Fracture deflecting propagation follows the step-by-step mixed-mode (I-II) fracturing mode. The proposed model is applicable to each fracture propagation step (Figure 1(b)). In each propagation step, the FPZ (cohesive crack) growth direction follows the maximum tensile (tangential) criteria [9, 31, 32] at the initial mixed-mode fracture tip and the completely developed FPZ tip (cohesive crack tip)

(3) In each propagation step of mixed-mode fracturing, the FPZ growth path and the subsequent real fracture (stable and unstable) propagation trajectory are supposed to be straight, based on the experimental results (Figure 2)

Note that the maximum tensile (tangential) criteria will not be discussed in detail. It is not the goal of this work. The HF deflecting extension trajectory depends on the rate-dependent mixed-mode (I-II) fracture propagation distance in each step, which will be interpreted in Section 3. This model is mainly used to deeply analyze the correlation between the fracture driving force and resistance, providing theoretical bases for revealing the injection rate-dependent deflecting propagation rule of hydraulic fracture.

The tensile FPZ development is seen as the nucleation and coalescence of the microcracks with energy dissipation in the vicinity of a crack tip [21, 27, 33]. At different loading rates, materials softening in FPZ due to the generation of microcracks (Figure 4(a)) can be delineated by the softening opening of cohesive crack ahead of the mixed-mode (I-II) crack tip (Figure 4(b)). Along the cohesive crack, cohesive stress is distributed and tends to close the crack (Figure 4(b)), eliminating the singularity at the cohesive crack tip. Cohesive stress decreases with the softening deteriorating, which can be represented by the relationship between the cohesive stress (σ_c) and the crack opening displacement (COD; w) in a unit area of cohesive crack (Figure 4(c)). Considering the moderate softening in FPZ, the σ_c-w curve of most rock-like materials is supposed to be linear (Figure 4(c)) [22, 34, 35]. At a constant loading rate, the softening function of σ_c-w follows Equation (1).

$$\sigma_c(w) = \sigma_t - \left(\frac{\sigma_t}{w_{cmax}}\right)w, \qquad (1)$$

where σ_c is the cohesive stress, w the crack opening displacement (COD), σ_t the cohesive tensile strength, and w_{cmax} the critical COD.

When σ_c on both sides of the FPZ reaches σ_t, the cohesive crack begins to soften, indicating that the FPZ starts to develop (Figure 4(c)). Then, σ_c decreases with the increment of COD. When σ_c vanishes and COD reaches the critical value (w_{cmax}), the real fracture surface of a unit area generates, and FPZ develops completely. The area under the softening curve is the dissipated energy (G_f) (Equation (2)), which is equal to the cohesive fracture energy (G_F) (Equation (3)) when the crack faces are completely separated
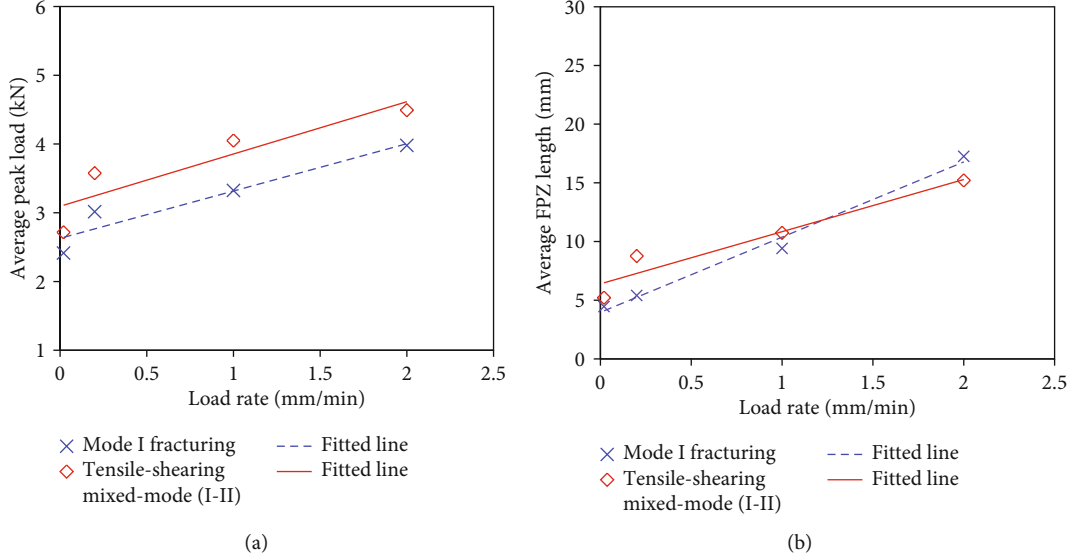
FIGURE 3: The evolution law of FPZ length and peak load with loading rates increasing: (a) peak load vs. loading rates; (b) FPZ length vs. loading rates.

(Figure 4(c)).

$$G_f(y_1) = \int_0^{w(y_1)} \sigma_c(w)dw, \qquad (2)$$

$$G_F = \int_0^{w_{cmax}} \sigma_c(w)dw. \qquad (3)$$

As shown in Figures 2 and 3, FPZ length is remarkably increased with the rising quasistatic loading rate. The completed development FPZ length (L) is regarded as the prominent rate-dependent parameter [28]. Therefore, distributions of cohesive stress and COD along the FPZ are rate-dependent (Equations (4)–(6)), and the $G_f(y_1)$ in Equation (2) is also rate-dependent. The previous experimental investigations [27, 29, 30, 36] validate that σ_c and w are linearly (Figure 4(d)) distributed along the FPZ (Equations (4) and (5)) and w_{cmax} is linearly (Figure 4(e)) increased with developing FPZ length (l) (Equation (5)).

$$\sigma_c(y_1, r) = \sigma_c(w(y_1, r)) - \left[\frac{\sigma_c(w(y_1, r))}{l}\right]y_1, \qquad (4)$$

$$w(y_1, r) = w_c(l, r) - \left[\frac{w_c(l, r)}{l}\right]y_1, \qquad (5)$$

$$w_c(l, r) = \left[\frac{w_{cmax}}{L(r)}\right]l, \qquad (6)$$

where y_1 is the axis along FPZ develop direction, r the loading rate, l the developing FPZ length, L the length of a completely developed FPZ, and w_c the crack tip opening displacement (CTOD).

In each fracture propagation step, the accumulated dissipated energy (G_d) in FPZ can be obtained by the integration of $G_f(y_1)$ along the FPZ length (Equation (7)). $G_d(l)$ can be regarded as the fracture resistance during the cohesive crack extending. When the FPZ develops completely; i.e., $l = L$, G_f reaches the critical value, G_D, which is a function of the rate-dependent FPZ length, as presented in Equation (8). G_D indicates the fracture resistance of FPZ completely developing, corresponding to generating the real mixed-mode (I-II) fracture of a unit area at the tip of an initial crack tip without FPZ.

$$G_d(r, l) = \int_0^l G_f(r, y_1)dy_1, \qquad (7)$$

$$G_D(r) = \int_0^{L(r)} G_f(r, y_1)dy_1. \qquad (8)$$

Substitution of Equations (1)–(6) into Equations (7) and (8) yields

$$G_d(r, l) = \frac{\left[w_{cmax}\sigma_t(3L(r) - 2l)l^2\right]}{6L^2(r)}, \qquad (9)$$

$$G_D(r) = \frac{\left[w_{cmax}\sigma_t L(r)\right]}{6}. \qquad (10)$$

As mentioned above, the completed development FPZ length (L) is the prominent rate-dependent parameter [28] of FPZ development during mixed-mode (I-II) fracturing. As presented in Equations (9) and (10), the effect of loading rates on G_d and G_D depends on $L(r)$. Therefore, we can obtain two rate-dependent fracture resistance indexes (including FPZ length) via dividing Equations (9) and (10) by $w_{cmax}\sigma_t$, as listed in Equations (11) and (12).

$$R_d(r, l) = \frac{G_d(r, l)}{(w_{cmax}\sigma_t)} = \frac{\left[(3L(r) - 2l)l^2\right]}{\left[6L^2(r)\right]}, \qquad (11)$$
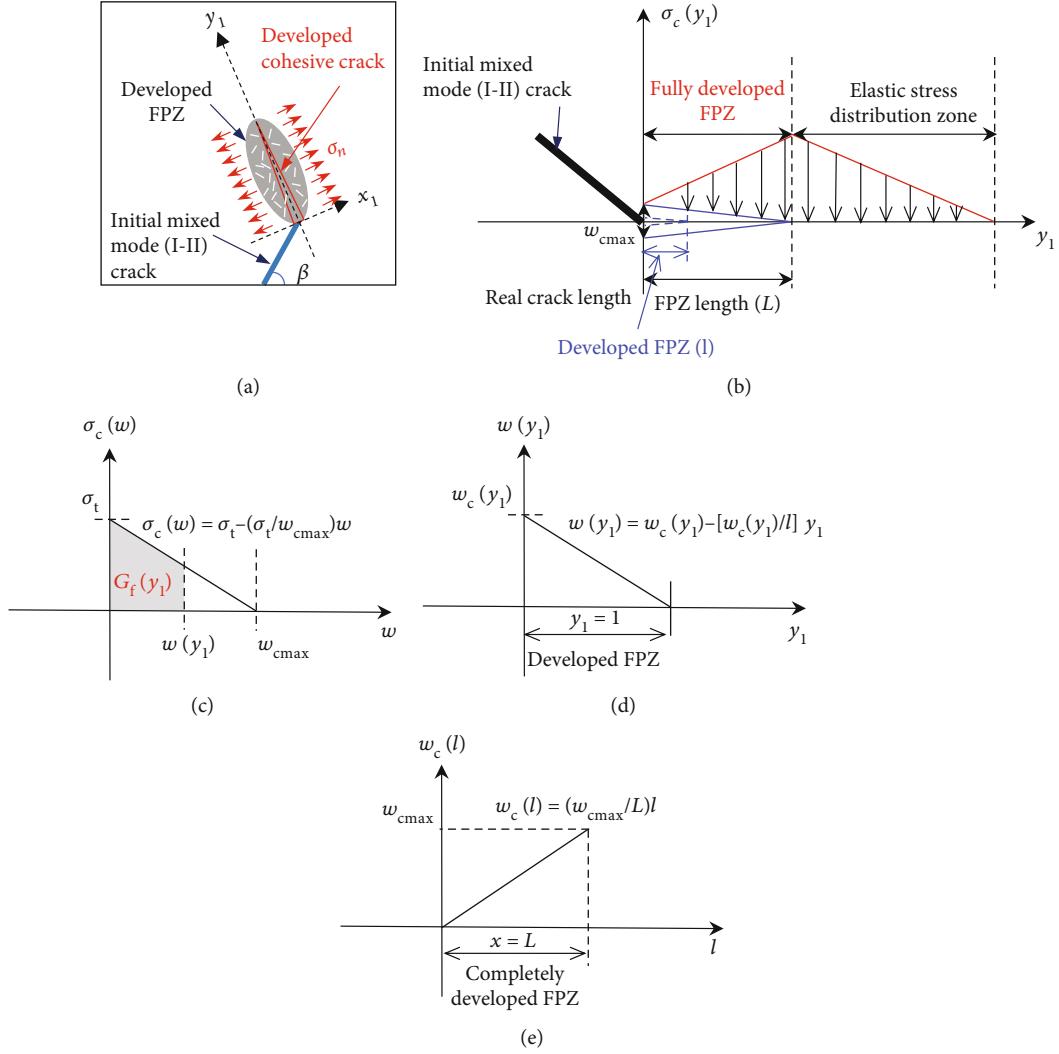
FIGURE 4: FPZ Development ahead of the mixed-mode (I-II) fracture tip of rock-like materials: (a) schematic diagram of the tensile development of the FPZ under mixed-mode (I-II) stresses; (b) cohesive stresses distributed along the cohesive crack in FPZ, ahead of the mixed-mode (I-II) fracture tip; (c) cohesive stress vs. crack opening displacement; (d) the distribution of crack opening displacement along the cohesive crack (i.e., FPZ); (e) the rising crack tip opening displacement with FPZ development (i.e., the increment of FPZ length).

$$R_D(r, L) = \frac{G_D(r)}{(w_{cmax}\sigma_t)} = \frac{L(r)}{6}, \tag{12}$$

where R_d and R_D are rate-dependent fracture resistance indexes corresponding to the developing and completely developed FPZ length.

Equations (11) and (12) present the fracture resistance during FPZ developing ahead of the real mixed-mode (I-II) fracture tip (i.e., the mixed-mode fracture initiation). The classical rock fracture mechanics indicates that the real fracture generation and extension are supposed to be quasistatic after FPZ completely developing [31, 36–38]. More specifically, once the FPZ develops completely, a new and real fracture surface per unit length will generate in FPZ ahead of the initial fracture tip. Due to the continuous nucleation and coalescence of microcracks in FPZ at the real fracture tip, the completely developed FPZ always locates at the extending real fracture tip. Namely, the real mixed-mode (I-II) fracture

pushes the tensile FPZ to propagate. Therefore, under the condition of stable fracture propagation, G_F is the stable fracture resistance of generating a real fracture surface per unit area after FPZ completely developing. Substituting Equation (1) into Equation (3), the expression of G_F follows

$$G_F = \frac{(w_{cmax}\sigma_t)}{2}. \tag{13}$$

Similar to Equations (11) and (12), the rate-dependent fracture resistance index (R_F) corresponding to G_F follows

$$R_F(r, a) = \frac{G_F}{(w_{cmax}\sigma_t)} = \frac{1}{2}, \tag{14}$$

where a is the real fracture length. Note that R_F is independent of FPZ length and less than R_D, with the unit of mm. Note that the difference between R_F and R_D is rate-

dependent, which significantly correlated to fracture deflecting propagation and will be discussed in detail in Section 2.2.

2.2. Model-Based Rate-Dependent Stable and Unstable Propagation of Mixed-Mode (I-II) Fractures.

The relationship between the fracture driving force (stress or energy driving fracture propagation) and fracture resistance determines the stable and unstable propagation of the mixed-mode (I-II) fracture [31, 32, 37]. Note that the FPZ developing process is stable [22, 34, 35] and the stable or unstable fracture propagation occurs after FPZ developing to be the real fracture surface. In this section, we will analyze the rate-dependent stable and unstable propagation based on the proposed mixed-mode (I-II) fracture model.

2.2.1. Rate-Dependent Stable Propagation of the Mixed-Mode (I-II) Fracture.

The stable fracture propagation follows that the fracture driving force equals fracture resistance [31, 32, 37], as in Equation (15). In each fracture extension step, FPZ ahead of the mixed-mode (I-II) fracture tip is the dominant fracture propagation path, and the real fracture surface stably generates in FPZ. Therefore, FPZ length is the fracture propagation distance in each crack extension step.

$$
\begin{cases}
D_F(r, l) = R_d(r, l) = \dfrac{\left[(3L(r) - 2l)l^2\right]}{\left[6L^2(r)\right]} & \text{FPZ development,} \\[4mm]
D_F(r, a) = R_F(r, a) = \dfrac{1}{2} & \text{real fracture propagation,}
\end{cases}
\tag{15}
$$

where D_F is the driving force. As presented in Equation (15), once the FPZ develops completely, the fracture resistance $R_d(r, l)$ will reduce to $R_F(r, a)$, and the real fracture surface begins to generate in FPZ. Given the above discontinuity of fracture resistance, the driving force should reduce from $D_F(r, l)$ to $D_F(r, a)$ as in Equation (15), keeping the balance between the driving force and the fracture resistance. The overlapped driving force and resistance curve are shown in Figure 5.

As shown in Figure 5, the negative horizontal axis indicates the FPZ development, where the reduction of $l - L$ represents FPZ propagation ahead of the mixed-mode (I-II) fracture. The positive horizontal axis means the real fracture extension (Δa). Under different quasistatic loading rates, Figure 5 shows that only the fracture resistance in FPZ development is rate-dependent; in contrast, the generation of real fracture surfaces after FPZ completely developing is constant. Therefore, the resistance curves at different quasistatic loading rates overlap with the increment of real fracture surfaces.

At different quasistatic loading rates, the stable propagation of the mixed-mode (I-II) fracture divides into four stages. Take the overlapped curves of driving forces and fracture resistances at a loading rate of 2 mm/min as an example. (1) Stage A-B represents the FPZ (FPZ$_1$) development, where points A and B represent the initial and completed development of the tensile FPZ (FPZ$_1$) ahead of the mixed-mode (I-II) fracture tip. (2) Stage B-C indicates the transition from FPZ (i.e., cohesive crack) development to the real fracture

generation. More specially, when the fracture resistance reaches point C, the real fracture of a unit area generates, and the fracture resistance sharply decreases. To maintain the fracture propagates stably, the driving force should reduce from point A to point B, consistent with the fracture resistance. Since FPZ$_1$ grows completely, a new FPZ (FPZ$_2$) starts to develop at the tip of FPZ$_1$, i.e., the cohesive crack tip perpendicular to the maximum tensile stress. (3) Stage C-D delineates the stable propagation of a real fracture. When Δa attains to L, FPZ develops to be a real fracture surface, and FPZ$_2$ grows completely along a new direction. Since the FPZ length is a material property at a constant loading rate, the length of FPZ$_1$ is equal to FPZ$_2$.

Note that the deflecting propagation of the mixed-mode fracture will repeat stage C-D once the real fracture length exceeds L. Namely, the stable deflecting propagation follows step-by-step and polyline-mode. The propagation distance in each step is the rate-dependent FPZ length of the mixed-mode (I-II) fracture.

2.2.2. Rate-Dependent Unstable Propagation and Arrest of the Mixed-Mode (I-II) Fracture.

Usually, the increasing real fracture length tends to improve the driving force [38], which will increase the difficulty of keeping the balance between the driving force and the fracture resistance during mixed-mode (I-II) fracturing. Therefore, the fracture tends to propagate unstably once the FPZ develops completely. In this part, the rate-dependent unstable propagation and arrest of the mixed-mode (I-II) fracture will be analyzed.

When the fracture length increases and the driving force has no sufficient time to unload, the driving force will be larger than the fracture resistance, which will lead to the unstable propagation of the mixed-mode (I-II) fracture (Equation (16)). Once the fracture propagates unstably, the kinetic energy (Equation (17)) generates and drives the fracture extension [37], though the driving force is less than fracture resistance (Equation (16) and Equation (18)). Once the fracture resistance depletes the kinetic energy (Equation (19)), the unstable fracture will stop extending (i.e., fracture arrest). Consequently, the kinetic energy (driving force minus resistance, such as the integrated area of S_{BCHE} and S_{GCHF} in Figure 6) of unstable fracture propagation can be regarded as another type of driving force. The above unstable propagation of mixed-mode (I-II) fracture will be illustrated in detail in Figure 6, a simplified schematic diagram of FPZ development, unstable fracture propagation, and fracture arrest at different loading rates.

$$
\begin{cases}
D_F(r, l) = R_d(r, l) = \dfrac{\left[(3L(r) - 2l)l^2\right]}{\left[6L^2(r)\right]} & \text{stable development of FPZ,} \\[4mm]
D_F(r, a) > R_F(r, a) = \dfrac{1}{2} & \text{unstable propagation of the real fracture,} \\[4mm]
D_F(r, a) < R_F(r, a) = \dfrac{1}{2} & \text{fracture arrest,}
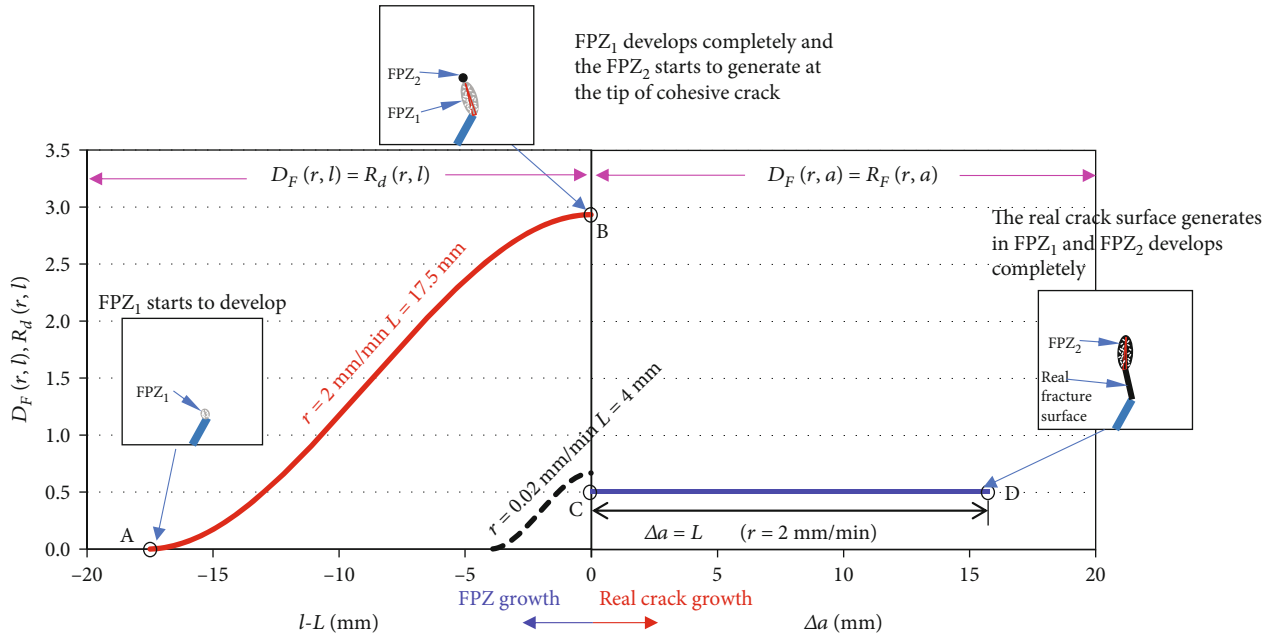\end{cases}
\tag{16}
$$

Figure 5: Schematic diagram of fracture resistance and driving force curves of the stable propagation of mixed-mode cracks at different loading rates.
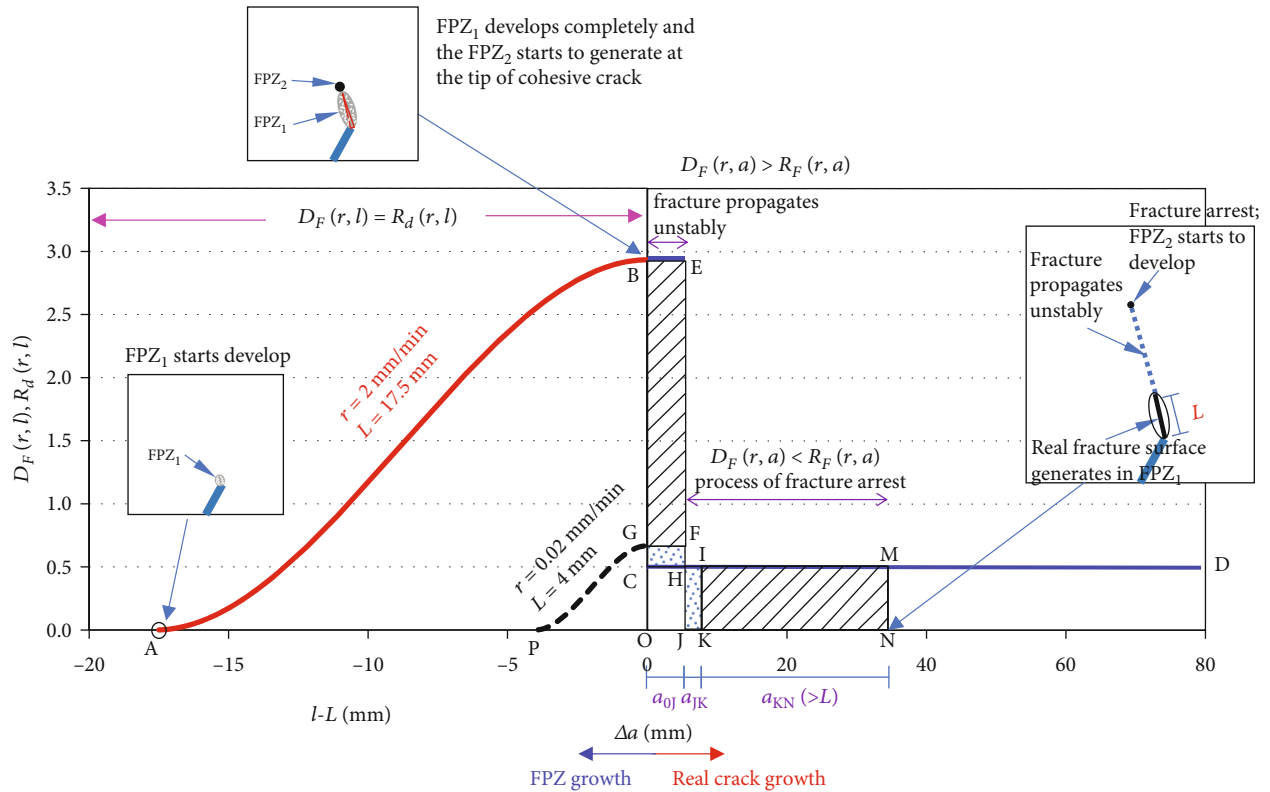

Figure 6: Schematic diagram of fracture resistance and driving force curves corresponding to the unstable propagation of mixed-mode cracks at different loading rates.

$$E_{\text{kin}} = \int_{a_0}^{a_0 + \Delta a_1} [D_{\text{F}}(r, a) - R_{\text{F}}(r, a)] \mathrm{d}a, \qquad (17)$$

where E_{kin} is the kinetic energy due to unstable fracture propagation, a_0 the initial real fracture length, and Δa_1 the unstable propagation distance of the real fracture under $D_{\text{F}}(r, a) > R_{\text{F}}(r, a)$.

$$E_{\text{arr}} = \int_{a_0 + \Delta a_1}^{a_0 + \Delta a_1 + \Delta a_2} [R_{\text{F}}(r, a) - D_{\text{F}}(r, a)] \mathrm{d}a, \qquad (18)$$

where E_{arr} is the depleting energy of fracture arrest and Δa_2 is the unstable propagation distance of the real fracture under arrest process.

$$E_{\text{kin}} = E_{\text{arr}}. \qquad (19)$$

The unstable propagation and arrest of the mixed-mode (I-II) fracture are mainly due to the fracture resistance discontinuity between the FPZ development and the real fracture generation. More specially, as shown in Figure 6, when the overlapped driving force and fracture resistance reach point B, FPZ develops completely, and the real fracture surface begins to generate. With the increment of loading rates, the fracture resistance discontinuity, such as the segment B-C and the segment G-C, presents more remarkably. Based on this, usually, the driving force is hard to decrease in time and keep balance with the sharply reduced fracture resistance

[37]. Therefore, the mixed-mode (I-II) fracture tends to propagate unstably, which is more remarkable at the high loading rate. Once the balance between the driving force (segment B-E and segment G-F in Figure 6) and the fracture resistance (segment C-H in Figure 6) is broken, the fracture begins to propagate unstably. Then, kinetic energies generate and can be delineated by the integrated area (Equation (20)) of S_{BCHE} and S_{GCHF} (Figure 6). Based on the previous investigation [38], unloading occurs with the sudden generation of real fracture surfaces, and driving forces will decrease less than the fracture resistance. For instance, segments E-J and F-J correspond to the decreased driving fore at loading rates of 2 mm/min and 0.02 mm/min, respectively. The rate-dependent fracture unstable propagation begins to arrest when the driving force is less than fracture resistance. Until E_{arr} depletes E_{kin} (Equations (17)–(19)) at different loading rates, the mixed-mode (I-II) fracture arrests completely. More specifically, as shown in Figure 6, at the loading rate of 0.02 mm/min, when S_{HJKI} (E_{arr}) is equal to S_{GCHF} (E_{kin}), fracture arrests completely. Similarly, at the loading rate of 2 mm/min, the arrest of the unstable propagation of the mixed-mode (I-II) fracture should fulfill $S_{\text{HJNM}} = S_{\text{BCHE}}$. Then, the fracture will propagate along a new direction in the next step, repeating the driving force evolution of segment ABEJKN (at 2 mm/min) and segment PGFJN (at 0.02 mm/min), i.e., the cycle of FPZ development, unstable fracture propagation, and fracture arrest.

$$\begin{cases} E_{\text{kin}} = \int_0^{a_{0\text{J}}} [D_{\text{F}}(2, a) - R_{\text{F}}(2, a)] \mathrm{d}a = S_{\text{BCHE}} = E_{\text{res}} = \int_{a_{0\text{J}}}^{a_{\text{JK}} + a_{\text{KN}}} R_{\text{F}}(2, a) \mathrm{d}a = S_{\text{HJNM}} \text{ high loding rate,} \\ \\ E_{\text{kin}} = \int_0^{a_{0\text{J}}} [D_{\text{F}}(0.02, a) - R_{\text{F}}(0.02, a)] \mathrm{d}a = S_{\text{GCHF}} = E_{\text{res}} = \int_{a_{0\text{J}}}^{a_{\text{JK}}} R_{\text{F}}(0.02, a) \mathrm{d}a = S_{\text{HJKI}} \text{ low loading rate.} \end{cases} \qquad (20)$$

The above analyses indicate E_{kin} at the high loading rate is larger than that at the low loading rate. Namely, the increased loading rate will aggravate the unstable fracture propagation. As shown in Figure 6, $(a_{\text{JK}} + a_{\text{KN}})$ at a high loading rate of 2 mm/min is remarkably longer than a_{JK} at a low loading rate of 0.02 mm/min.

2.2.3. Comparison between the Rate-Dependent Stable and Unstable Propagation of the Mixed-Mode (I-II) Fracture. As shown in Figure 7, both the stable and unstable deflecting propagations of the mixed-mode (I-II) fracture follow step-by-step and polyline-mode (HF propagation trajectory presents a polyline shape). With the increment of loading rate, the discontinuity of fracture resistance corresponding to the completed development of FPZ increases significantly, which extends the propagation distance in each extension step of mixed-mode (I-II) fracturing. The velocities (about 0.38 sound velocity at this material) of fracture unstable propagation and arrest are significantly faster than that at quasistatic

propagation conditions [37]. Therefore, the propagation distance of the mixed-mode (I-II) fracture at each extension step is remarkably longer than the FPZ length (i.e., the stable fracture propagation distance in each step), as shown in Figure 7.

Based on the above theoretical analyses, the propagation distance of mixed-mode (I-II) fracture in each extension step will determine the fracture deflecting propagation trajectory, regardless of fracture stable or unstable propagation. The detailed analyses will present in Section 3.

3. Injection Rate-Dependent Deflecting Propagation Rules of the Hydraulic Fracture

The injection of fracturing fluid is the loading approach of hydraulic fracturing. Based on the proposed rate-dependent mixed-mode (I-II) fracture model; in this section, we will propose the injection rate-dependent (IRD) HF deflecting propagation modes.
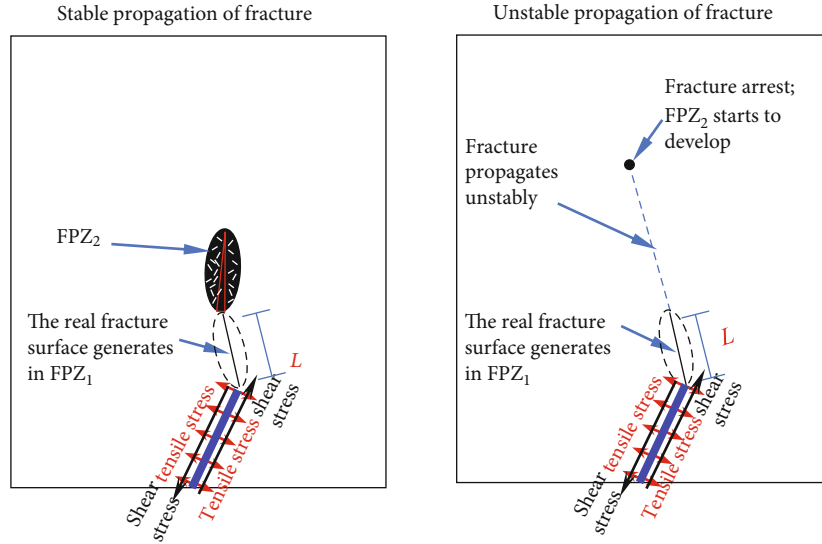
FIGURE 7: Comparison between stable and unstable propagations of mixed-mode fracturing.

As shown in Figure 1(b), for the microelement of the deflecting HF oblique to the principal stresses, the in situ stresses provide the normal stress (closing the fracture surface) and the shear stress. Once the pressure (p) of fracturing fluid inside the fracture surface offsets the normal closing stress and reaches the critical cohesive tensile strength, the tensile FPZ and real fracture surface propagate in sequence at the mixed-mode (I-II) cohesive crack tip (the tip of a completely developed FPZ in the last extension step). Note that based on the maximum tangential stress criteria [9, 31, 32], the fracture initiation direction depends on the ratio of tensile stress intensity factor to shear stress intensity, i.e., $K_{\mathrm{I}}/K_{\mathrm{II}}$, at both the real and nominal crack (such as cohesive crack) tips. Consequently, the fracture propagation direction at each step is independent of the fracture length [3, 9]; i.e., the deflecting angle changes barely at each fracture propagation step. Furthermore, the HF deflecting trajectory is dependent on the fracture propagation distance in each step. The longer the fracture propagation distance in each step is, the larger the HF deflecting radius is. In the next context, we will analyze the injection rate-dependent HF stable and unstable deflecting propagations, respectively. As this research focuses on the rate-dependent mixed-mode (I-II) fracturing behavior of HF deflecting propagation, the flow and seepage characteristics of the fracturing fluid are not the goal of this work.

3.1. Injection Rate-Dependent HF Stable Deflecting Propagation Mode. As shown in Figure 8, β is defined as the angle between the prefabricated fracture (formed by directional slotting or directional perforating) and the direction of minimum in situ stress (σ_3). Considering that the in situ stresses, β and deflecting angle in each step are constant, the overlapped driving force and fracture resistance during stable fracture propagations follow the evolution law as in Figure 5 at different loading rates. The fracture extension distance in each propagation step is consistent with the FPZ length.

Figures 8(a) and 8(b) show that the HF deflecting trajectory or deflecting radius is significantly increased with the rising fluid injection rate, which is due to the extended FPZ length at the fast fluid injection. In detail, under the fracture stable propagation condition, the real fracture stably generates along the FPZ. Thus, the FPZ length is the HF deflecting propagation distance in each step. When the HF deflecting propagation steps are constant, the increased FPZ length at high injection rates will raise the HF deflecting propagation trajectory, i.e., the HF deflecting propagation radius. By analogy, the turning radius of a car depends on the length of the body. To better interpolate the HF stable deflecting propagation rule, the HF stable deflecting propagation trajectory is similar to a car turning. The turning radius is dependent on the car body length, which is corresponding to the FPZ length of HF stable deflecting propagation. In this work, the HF stable deflecting propagation modes at the low and high injection rates are defined as mode 1-1 and mode 1-2, as shown in Figures 8(a) and 8(b).

3.2. Injection Rate-Dependent HF Unstable Deflecting Propagation Mode. As mentioned above, when the mixed-mode (I-II) crack propagates unstably in each step, the extension distance of the real fracture is supposed to be longer than that of stable fracture propagation due to the high velocity [37] of the unstable fracture propagation. Consequently, under the constant loading rate, the HF deflecting extension distance during unstable propagation and arrest in each step (Figures 8(c) and 8(d)) will be much longer than that of stable fracture propagation (Figures 8(a) and 8(b)).

Based on the evolution rule of the unstable fracture propagation and arrest as in Figure 6, the fracture resistance discontinuity of FPZ developing to be a real fracture surface is increased with the rising loading rate, such as the segment BC and segment GC in Figure 6. The increasing resistance discontinuity (from FPZ development to real fracture generation) with a rising loading rate will improve the kinetic energy of HF unstable propagation. Then, the distance of
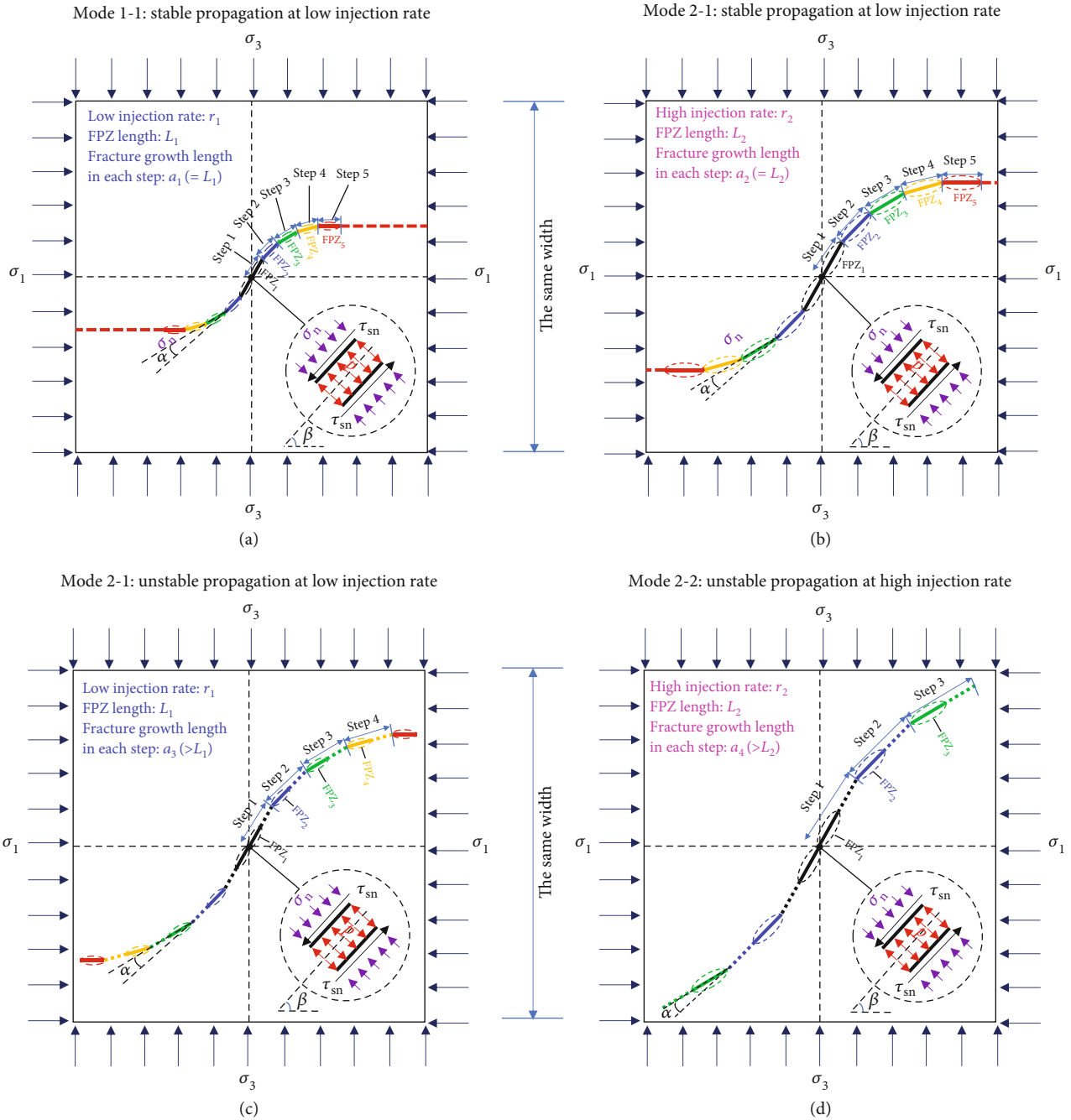
Figure 8: Injection rate-dependent deflecting propagation (conceptual) mode of the hydraulic fracture (for r and L, subscripts 1 and 2 correspond to low and high injection rates, respectively; the subscripts of a correspond to the propagation mode, such as modes 1-1, 1-2, 2-1, and 2-2): (a) (mode 1-1) stable propagation at the low injection rate; (b) (mode 1-2) stable propagation at the high injection rate; (c) (mode 2-1) unstable propagation at the low injection rate; (d) (mode 2-2) unstable propagation at the high injection rate.

HF unstable propagation will increase in each deflecting extension step (Figures 8(c) and 8(d)), driven by the increased kinetic energy. Consequently, within the limited extension steps, the deflecting HF will extend over a longer deflecting distance or a larger deflecting radius at a high injection rate. The deflecting HF tends to propagate along the designed initial fracture direction, such as Figure 8(d). At low and high fluid injection rates, the unstable propaga-

tion and arrest of the deflecting HF are defined as mode 2-1 (Figure 8(c)) and mode 2-2 (Figure 8(d)), respectively.

Figure 8 indicates that deflecting HF oblique to the in situ stresses tends to propagate along the initial fracture direction under mode 2-2; i.e., deflecting HF propagates unstably at high fluid injecting rates. In contrast, deflecting HF is hard to maintain the initial fracture direction under stable propagation at a low injection rate, such as mode 1-1.
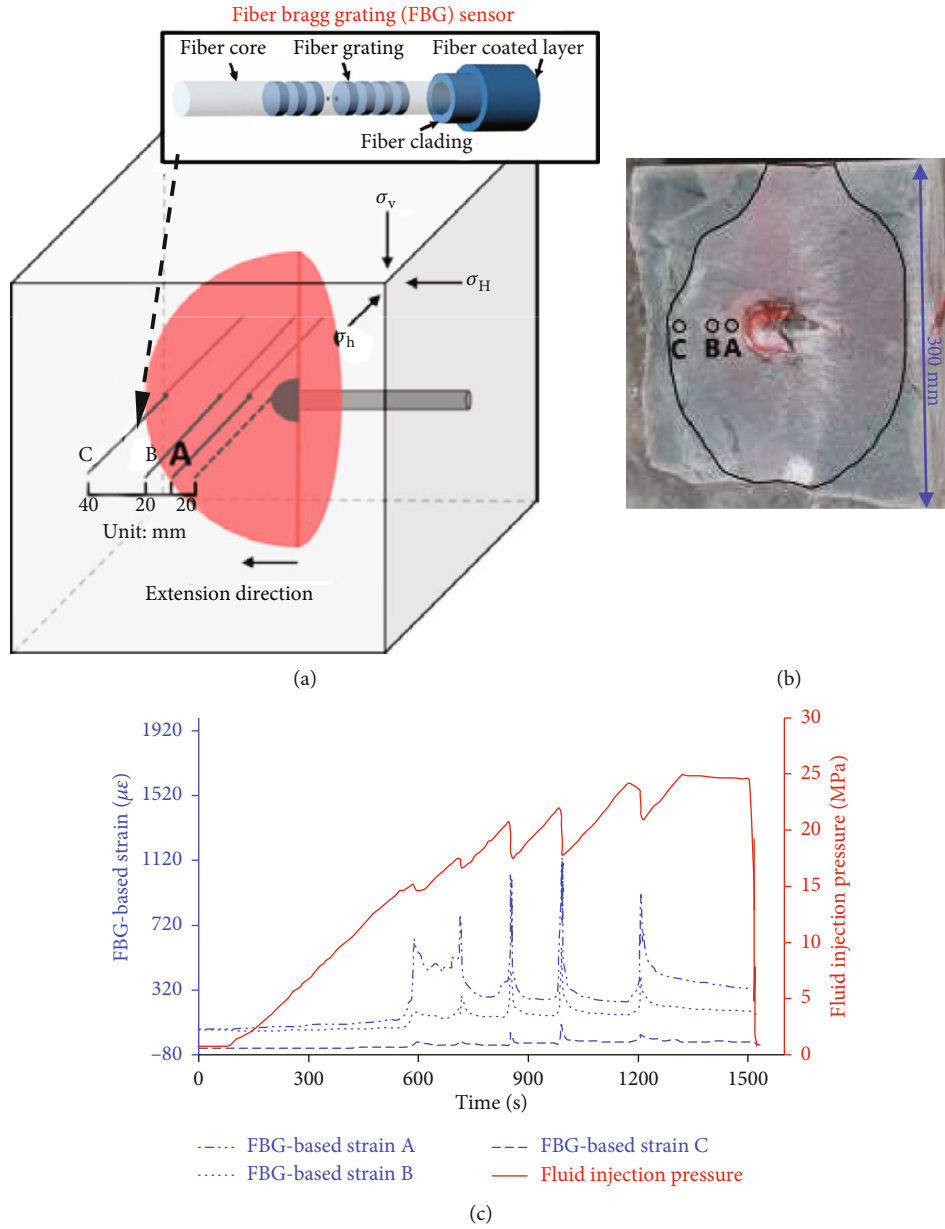
(a)

(b)

(c)

FIGURE 9: Hydraulic fracture propagation characterized by Fiber Bragg Grating (FBG) sensors (replotted based on the experimental results of Yang et al. [39]): (a) the layout of FBG sensors; (b) hydraulic fracture surface; (c) FBG-based strains and injection pressures.

TABLE 1: Experimental programs of deflecting propagation of hydraulic fracture.

Group	Principal stresses (MPa)			The angle between prefabricated crack and σ_h (°)	Fluid injection rate (ml/s)
	σ_v	σ_H	σ_h		
1	10	9	6	45	1.0
2	10	9	6	45	1.5
3	10	9	6	45	5.0

4. Experimental Validations of the Theoretical IRD HF Deflecting Propagation Mode

In this section, the IRD HF deflecting propagation mode mentioned above will be validated by the published physical simulations [8–39] of hydraulic fracturing.

4.1. Validations of the Step-By-Step Propagation of the Hydraulic Fracture. The HF deflecting extension modes in Section 3 are proposed on the premise of the HF step-by-step propagation, whether the mixed-mode (I-II) fracturing is stable or unstable. As mentioned above, the fracture type is tensile ahead of the mixed-mode (I-II) fracture tip at different quasistatic loading rates. In this part, the tensile propagation characteristics (published by Yang et al. 2017 [39]) of the
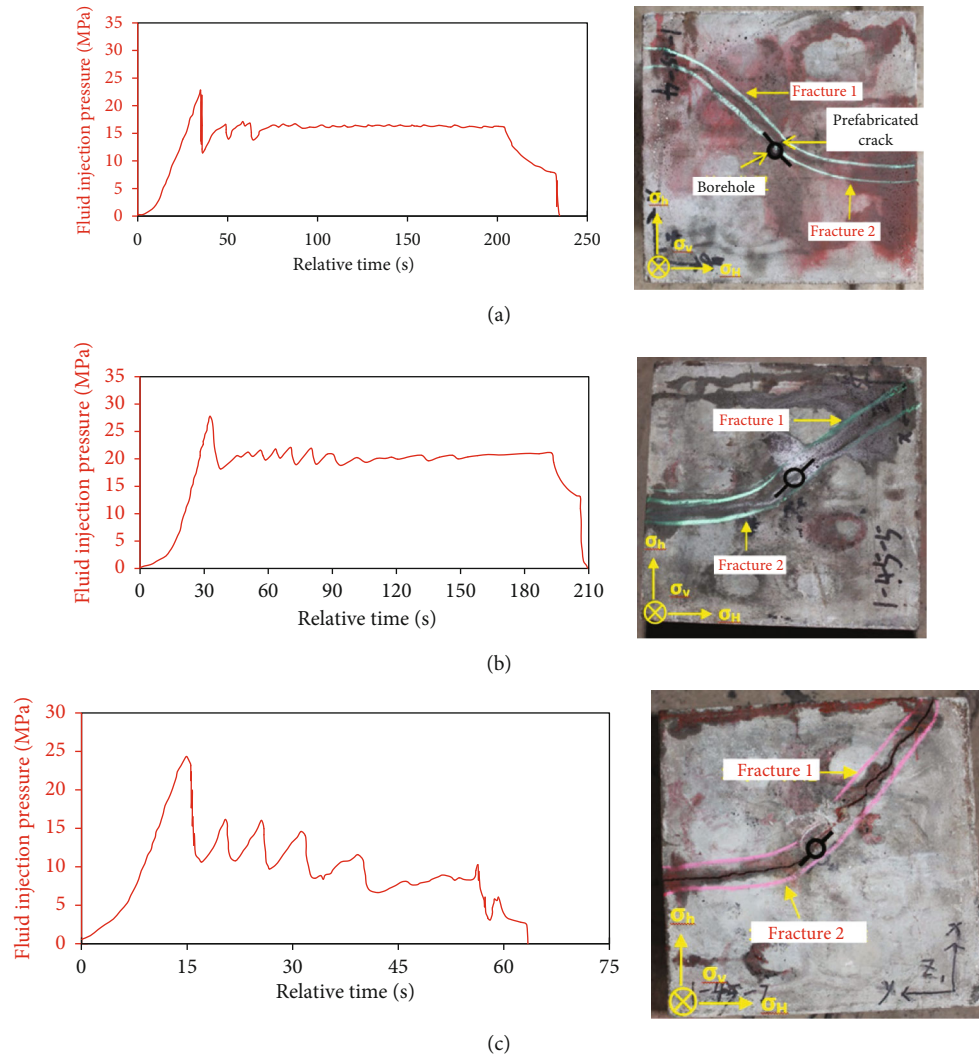
FIGURE 10: Injection pressure curves and deflecting HF geometries at different injection rates (replotted based on the experimental results of Lin et al. [8]): (a) 1.0 ml/s; (b) 1.5 ml/s; (c) 5.0 ml/s.

hydraulic fracture, detected with Fiber Bragg Grating (FBG), are employed to validate the step-by-step extension of the proposed IRD HF propagation mode.

Yang et al. [39] prefabricated three FBG sensors along the hydraulic fracture propagation path in the artificial concrete specimen, as shown in Figures 9(a) and 9(b). FBG sensors were used to identify the opening width (represented by the strain) and propagation rate of the hydraulic fracture in real time. The triaxial confining stress applied to the specimen is 9 MPa (σ_3), 15 MPa (σ_2), and 17 MPa (σ_1). The initial fracturing direction was perpendicular to the minimum principal stress at the center of the sample (Figure 9(b)). The fracturing fluid with a viscosity of 107 mPa·s was injected with a low rate of 2 ml/min, driving the hydraulic fracture propagation. The red dye was added to the fracturing fluid to identify the hydraulic fracture surface (Figure 9(b)). Based on the previous investigations [5, 8, 26], the red dye changes the fracturing fluid very slightly, and adding guar gum is the remarkable and widely used approach for increasing the fracturing fluid viscosity. Since this work mainly investigates the effect of

fluid injection rate on fracture deflecting propagation, the relationship between fracturing fluid properties and hydraulic fracture propagation is not the goal of this work and will not be discussed in detail in this work. The geometry of the hydraulic fracture is approximately elliptical, as shown in Figure 9(b). The responses of injection pressure and FBG-based strain characterize the hydraulic fracture propagation. In detail, the injection pressure gradually rises and fluctuates (Figure 9(c)). Each time the injection pressure reaches the peak, then the injection pressure decreases rapidly, corresponding to the FBG-based strain of quick rising to the peak and then sharp dropping. As the fluid injection pressure can be regarded as the driving force of HF propagation, the sharp decrement of the injection pressure is corresponding to the driving force discontinuity as in Figures 5–6. The fluctuation intensity of the injection pressure curve is consistent with that of the FBG strain, which indicates the sharp fluctuation of injection pressure is supposed to be an index for qualitative characterizing HF extension distance in each step. The sequential responses of FBG sensors A, B, and C indicate
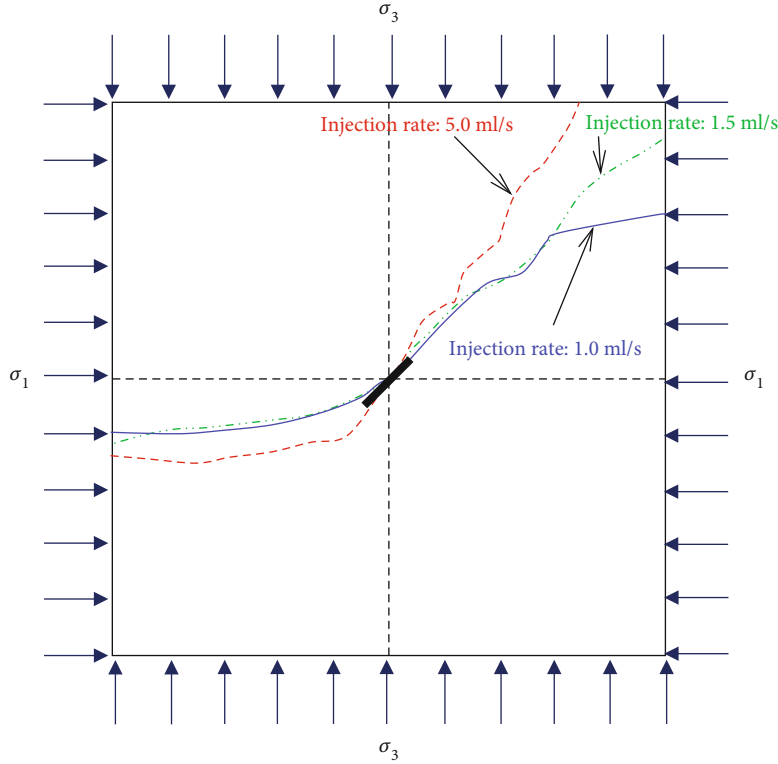
FIGURE 11: The comparison of the HF deflecting propagation trajectories at different loading rates.

the HF extension distance in each step is about 10~20 mm, at an injection rate of 2 ml/min. The above synchronous fluctuations of injection pressures and FBG-based strains validate that the HF propagates step-by-step (i.e., intermittently).

4.2. Validations of the Injection Rate-Dependent HF Deflecting Propagation Modes. In Section 4.1, the step-by-step propagation characteristics of the hydraulic fracture have been validated. On this basis, the injection rate-dependent HF deflecting propagation modes based on the proposed rate-dependent mixed-mode (I-II) fracturing model will be validated in this section, with the HF deflecting propagation tests published by Lin et al. [8].

Lin et al. [8] prepared the cube artificial concrete specimens (dimensions: 300 mm × 300 mm × 300 mm) to conduct hydraulic fracturing tests. At the center of the specimen, the initial crack with a 45° inclination angle to the minimum principal stress was prefabricated to make the hydraulic fracture deflecting propagation. The water with red dye was employed as the fracturing fluid. The red dye changes the fluid viscosity slightly, as indicated by the previous investigations [5, 8, 26]. Since the relationship between fracturing fluid properties and hydraulic fracture propagation is not the goal of this work, the effect of fracturing fluid properties on hydraulic fracture propagation will not be discussed in detail. The fracturing fluid was injected at different loading rates (1.0 ml/s, 1.5 ml/s, and 5.0 ml/s) to drive the deflecting hydraulic fracture extending. The experimental programs are shown in Table 1.

The HF geometries and injection pressures are presented in Figure 10. With the injection rate increasing from 1.0 ml/s to 5.0 ml/s, the fluctuation characteristics of the injection pressure curve present more and more significance. Given the fluctuation consistency of the injection pressures and the FBG-based strain (an index of HF opening width) as in Figure 9(c), the aggravated fluctuation of the injection pressure (Figure 10) is proportional to the HF propagation distance in a step; i.e., deflecting HF tends to unstable propagation and arrest after FPZ develops completely. Therefore, the extension distance of the deflecting HF in each step is increased with the rising injection rate; furthermore, the HF deflecting propagation at the injection rate of 5 ml/s is more in accord with the mode 2-2 as in Figure 9(d).

We compare the HF deflecting propagation trajectories (Figure 10) at different loading rates, as in Figure 11. With the injection rate increasing from 1.0 ml/s to 5.0 ml/s, the HF deflecting extension distance or radius increases significantly; i.e., the deflecting hydraulic fracture tends to propagate along the initially designed direction. Figures 10 and 11 indicate that the deflecting HF propagation mode follows the evolution of mode 1-1→mode 1-2→mode 2-1→mode 2-2 (Figure 8) with the fluid injection rate increasing, and the fast fluid injection tends to drive the deflecting propagating along the initially designed direction.

The above experimental results (Figures 10 and 11) are consistent with the theoretical IRD HF deflecting propagation mode (based on the proposed rate-dependent mixed-mode (I-II) fracture model of rock-like materials).

5. Discussion

This work theoretically investigated the injection rate-dependent deflecting propagation rule of hydraulic fracture, insights from the rate-dependent FPZ of mixed-mode (I-II) fracturing. We can qualitatively determine the key mechanism that the increasing FPZ length and the kinetic energy at high loading rates would improve the deflecting HF propagation distance in each extension step. Then the deflecting trajectory or the deflecting radius of the hydraulic fracture can be increased with the rising injection rate, such as the mode 2-2 in Figure 8. The above theoretical investigations can provide references for field applications in mining and oil-gas reservoir stimulations. (1) For hard roof weakening in mines, increasing the fluid injection rate can improve hydraulic fracture directional propagation along the designed direction, weakening the effect of disturbance stresses on the HF deflecting propagation. Then, the dynamic disaster such as the sudden collapse of the hard roof can be effectively prevented. (2) For oil/gas exploitation, rising injection rate can enhance the HF deflecting radius (i.e., type-S hydraulic fracture trajectory) of directional perforation hydraulic fracturing. Then the reservoir stimulation volume and the permeability can be improved.

The proposed rate-dependent mixed-mode (I-II) fracture model also has limitations. The fluid-solid coupling of hydraulic fracturing was not included in the rate-dependent mixed-mode (I-II) cohesive crack model proposed in this work. Therefore, the proposed model cannot characterize the injection rate-dependent HF deflecting propagation trajectory quantitatively. However, this work can provide references for the deep investigation of the injection rate-dependent hydraulic fracturing model.

6. Conclusions

(1) Given the increased length of the tensile FPZ ahead of the mixed-mode fracture tip at different loading rates, the rate-dependent mixed-mode (I-II) cohesive fracture model was proposed

(2) Based on the proposed model, the model-based rate-dependent stable and unstable propagation of mixed-mode (I-II) fractures were analyzed. Both the stable and unstable fracture deflecting propagations follow step-by-step and polyline-mode. Under stable fracture propagation, the propagation distance in each step is the rate-dependent FPZ length of the mixed-mode (I-II) fracture, and the FPZ length is increased with the increasing quasiloading rate. Under the unstable fracture propagation, the discontinuity of fracture resistance corresponding to the completed development of FPZ increases significantly with the rising loading rate. Due to the above rising discontinuity of fracture resistance at high injection rates, the fracture extension distance of unstable propagation and arrest is improved in each extension step during mixed-mode (I-II) fracturing

(3) The injection rate-dependent HF deflecting propagation modes were proposed. The rising fluid injection rate significantly increases the HF deflecting trajectory or deflecting radius, which is due to the increased HF propagation distance in each step. As the unstable fracture propagation velocity is significantly higher than that of stable propagation, the propagation distance of the deflecting HF in each extension step will be remarkably extended during the unstable propagation and arrest of the mixed-mode fracture. Therefore, the deflecting HF tends to propagate along the initially designed direction under unstable propagation conditions at high loading rates

(4) The model-based injection rate-dependent step-by-step deflecting propagation of the hydraulic fracture was validated by further processing of published true triaxial physical simulation tests of hydraulic fracturing. Furthermore, suggestions for controlling deflecting HF in field applications with the injection rate were discussed. The high injection rate can be employed to increase the deflecting trajectory or the deflecting radius of the hydraulic fracture. On this basis, the injection rate-dependent HF deflecting propagation rule can provide a basis for weakening the hard roof in mines with directional hydraulic fracturing and improving the stimulation volume of the type-S hydraulic fracture in the oil/-gas reservoir

Nomenclature

FPZ:	Fracture process zone
HF:	Hydraulic fracture
IRD:	Injection rate-dependent
XFEM:	Extended finite element method
COD, w:	Crack opening displacement (μm)
CTOD, w_c:	The crack tip opening displacement (μm)
σ_n:	Normal stress for closing HF (MPa)
τ_{sn}:	Shear stress of deflecting HF (MPa)
p:	Fluid injection pressure of hydraulic fracturing (MPa)
σ_c:	Cohesive stress (MPa)
σ_t:	Cohesive tensile strength (MPa)
w_{cmax}:	Critical COD (μm)
G_f:	Dissipated energy (MPa·mm^2)
G_F:	Cohesive fracture energy (MPa·mm^2)
G_d:	Fracture resistance during the cohesive crack extending (MPa·mm^2)
G_D:	Fracture resistance of FPZ developing completely (MPa·mm^2)
L:	The completely developed FPZ length (mm)
l:	The length of a developing FPZ (mm)
y_1:	The axis along FPZ develop direction (mm)
r:	Loading rate (MPa/s, mm/min, etc.)

$R_{\mathrm{d}}, R_{\mathrm{D}}$:	Rate-dependent fracture resistance indexes corresponding to the developing and completely developed FPZ length (mm)
R_{F}:	Rate-dependent fracture resistance index corresponding to the real fracture length (mm)
a:	Real fracture length (mm)
D_{F}:	Driving force corresponding to the FPZ length and the real fracture length (mm)
E_{kin}:	Kinetic energy due to unstable fracture propagation (mm^2; the unit is consistent with the integral area in the fracture resistance curve, as in Figure 6)
E_{arr}:	The depleting energy of fracture arrest (mm^2; the unit is consistent with the integral area in the fracture resistance curve, as in Figure 6)
a_0:	Initial real fracture length (mm)
Δa_1:	The unstable propagation distance of the real fracture (mm)
Δa_2:	The unstable propagation distance of the real fracture under arrest process (mm)
β:	The angle between the prefabricated fracture and the direction of minimum in situ stress (°)
$K_{\mathrm{I}}/K_{\mathrm{II}}$:	The ratio of tensile stress intensity factor to shear stress intensity (unit)
σ_3:	Minimum principal stress (MPa)
σ_2:	Intermediate principal stress (MPa)
σ_1:	Maximum principal stress (MPa)
step-by-step stable propagation mode:	At each fracture propagation step, the fracture extension is stable; i.e., driving force equals fracture resistance.
step-by-step unstable propagation mode:	At each fracture propagation step, the initial fracture propagation state is unstable; i.e., the driving force is higher than the fracture resistance.

Data Availability

The manuscript contains all the original data.

Conflicts of Interest

The authors declare that they have no conflicts of interest.

Acknowledgments

References

[1] B. X. Huang, Y. Z. Wang, and S. Cao, "Cavability control by hydraulic fracturing for top coal caving in hard thick coal seams," *International Journal of Rock Mechanics and Mining Sciences*, vol. 74, pp. 45–57, 2015.

[2] B. Huang, J. Liu, and Q. Zhang, "The reasonable breaking location of overhanging hard roof for directional hydraulic fracturing to control strong strata behaviors of gob-side entry," *International Journal of Rock Mechanics and Mining Sciences*, vol. 103, pp. 1–11, 2018.

[3] G. Q. Zhang and M. Chen, "Dynamic fracture propagation in hydraulic re-fracturing," *Journal of Petroleum Science and Engineering*, vol. 70, no. 3-4, pp. 266–272, 2010.

[4] J. Q. Deng, C. Lin, Q. Yang, Y. R. Liu, Z. F. Tao, and H. F. Duan, "Investigation of directional hydraulic fracturing based on true tri-axial experiment and finite element modeling," *Computers and Geotechnics*, vol. 75, pp. 28–47, 2016.

[5] Z. Y. Liu, Y. Jin, M. Chen, and B. Hou, "Analysis of non-planar multi-fracture propagation from layered-formation inclined-well hydraulic fracturing," *Rock Mechanics and Rock Engineering*, vol. 49, no. 5, pp. 1747–1758, 2016.

[6] Q. Gao, Y. F. Cheng, S. C. Han et al., "Exploration of non-planar hydraulic fracture propagation behaviors influenced by pre-existing fractured and unfractured wells," *Engineering Fracture Mechanics*, vol. 215, pp. 83–98, 2019.

[7] J. X. Li, S. M. Dong, W. Hua, Y. Yang, and X. L. Li, "Numerical simulation on deflecting hydraulic fracture with refracturing using extended finite element method," *Energies*, vol. 12, no. 11, p. 2044, 2019.

[8] J. Lin, C. Xu, and J. W. Yang, "Study on the influence of pump flow rate on the deflection of hydraulic fracturing cracks in longitudinal flume cutting," *Journal of China Coal Society*, vol. 45, no. 8, pp. 118–126, 2019.

[9] F. Erdogan and G. C. Sih, "On the crack extension in plates under plane loading and transverse shear," *Journal of Basic Engineering*, vol. 85, pp. 519–527, 1963.

[10] K. Palaniswamy and W. G. Knauss, "Propagation of a crack under general, in-plane tension," *International Journal of Fracture Mechanics*, vol. 8, no. 1, pp. 114–117, 1972.

[11] G. C. Sih, "Strain-energy-density factor applied to mixed mode crack problems," *International Journal of Fracture*, vol. 10, no. 3, pp. 305–321, 1974.

[12] A. Aminzadeh, A. Fahimifar, and M. Nejati, "On Brazilian disk test for mixed-mode I/II fracture toughness experiments of anisotropic rocks," *Theoretical and Applied Fracture Mechanics*, vol. 102, pp. 222–238, 2019.

[13] Z. P. Bažant and R. Gettu, "Rate effects and load relaxation in static fracture of concrete," *ACI Materials Journal*, vol. 89, no. 5, pp. 456–468, 1992.

[14] B. Mahanta, A. Tripathy, V. Vishal, T. N. Singh, and P. G. Ranjith, "Effects of strain rate on fracture toughness and energy release rate of gas shales," *Engineering Geology*, vol. 218, pp. 39–49, 2017.

[15] X. F. Li, X. Li, H. B. Li, Q. B. Zhang, and J. Zhao, "Dynamic tensile behaviours of heterogeneous rocks: the grain scale fracturing characteristics on strength and fragmentation," *International Journal of Impact Engineering*, vol. 118, pp. 98–118, 2018.

[16] Z. X. Zhang, S. Q. Kou, J. Yu, Y. Yu, L. G. Jiang, and P. A. Lindqvist, "Effects of loading rate on rock fracture," *International*

Journal of Rock Mechanics and Mining Sciences, vol. 36, no. 5, pp. 597–611, 1999.

[17] Q. B. Zhang and J. Zhao, "Effect of loading rate on fracture toughness and failure micromechanisms in marble," *Engineering Fracture Mechanics*, vol. 102, pp. 288–309, 2013.

[18] M. Ju, J. Li, J. Li, and J. Zhao, "Loading rate effects on anisotropy and crack propagation of weak bedding plane-rich rocks," *Engineering Fracture Mechanics*, vol. 230, article 106983, 2020.

[19] G. I. Barenblatt, "The formation of equilibrium cracks during brittle fracture. General ideas and hypotheses. Axially-symmetric cracks," *Journal of Applied Mathematics and Mechanics*, vol. 23, no. 3, pp. 622–636, 1959.

[20] D. S. Dugdale, "Yielding of steel sheets containing slits," *Journal of the Mechanics and Physics of Solids*, vol. 8, no. 2, pp. 100–104, 1960.

[21] K. Otsuka and H. Date, "Fracture process zone in concrete tension specimen," *Engineering Fracture Mechanics*, vol. 65, no. 2, pp. 111–131, 2000.

[22] Z. P. Bažant, "Concrete fracture models: testing and practice," *Engineering Fracture Mechanics*, vol. 69, no. 2, pp. 165–205, 2002.

[23] Q. Lin and J. F. Labuz, "Fracture of sandstone characterized by digital image correlation," *International Journal of Rock Mechanics and Mining Sciences*, vol. 60, pp. 235–245, 2013.

[24] B. Q. Li, B. Gonçalves da Silva, and H. Einstein, "Laboratory hydraulic fracturing of granite: acoustic emission observations and interpretation," *Engineering Fracture Mechanics*, vol. 209, pp. 200–220, 2019.

[25] N. Z. Liu, Y. S. Zou, X. F. Ma, N. Li, and S. Wu, "Study of hydraulic fracture growth behavior in heterogeneous tight sandstone formations using CT scanning and acoustic emission monitoring," *Petroleum Science*, vol. 16, no. 2, pp. 396–408, 2019.

[26] Y. K. Xing, G. Q. Zhang, T. Y. Luo, Y. W. Jiang, and S. W. Ning, "Hydraulic fracturing in high-temperature granite characterized by acoustic emission," *Journal of Petroleum Science and Engineering*, vol. 178, pp. 475–484, 2019.

[27] Y. K. Xing, G. Q. Zhang, B. Wan, and H. Zhao, "Subcritical fracturing of sandstone characterized by the acoustic emission energy," *Rock Mechanics and Rock Engineering*, vol. 52, no. 7, pp. 2459–2469, 2019.

[28] Y. K. Xing, B. X. Huang, E. Q. Ning, L. Zhao, and F. Jin, "Quasi-static loading rate effects on fracture process zone development of mixed-mode (I-II) fractures in rock-like materials," *Engineering Fracture Mechanics*, vol. 240, article 107365, 2020.

[29] J. F. Labuz, S. P. Shah, and C. H. Dowding, "Experimental analysis of crack propagation in granite," *International Journal of Rock Mechanics and Mining Science and Geomechanics Abstracts*, vol. 22, pp. 85–98, 1985.

[30] J. F. Labuz, S. P. Shah, and C. H. Dowding, "The fracture process zone in granite: evidence and effect," *International Journal of Rock Mechanics and Mining Science and Geomechanics Abstracts*, vol. 24, no. 4, pp. 235–246, 1987.

[31] B. K. Atkinson, *Fracture Mechanics of Rock*, Elsevier, 2015.

[32] T. L. Anderson, *Fracture Mechanics: Fundamentals and Applications*, CRC Press, 2017.

[33] E. N. Landis and L. Baillon, "Experiments to relate acoustic emission energy to fracture energy of concrete," *Journal of Engineering Mechanics*, vol. 128, no. 6, pp. 698–702, 2002.

[34] G. Zhang, Y. Xing, and L. Wang, "Comprehensive sandstone fracturing characterization: integration of fiber Bragg grating, digital imaging correlation and acoustic emission measurements," *Engineering Geology*, vol. 246, pp. 45–56, 2018.

[35] Q. Lin, B. Wan, Y. Wang, Y. H. Lu, and J. F. Labuz, "Unifying acoustic emission and digital imaging observations of quasi-brittle fracture," *Theoretical and Applied Fracture Mechanics*, vol. 103, article 102301, 2019.

[36] B. N. Whittaker, R. N. Singh, and G. Sun, *Rock Fracture Mechanics: Principles, Design, and Applications*, Elsevier, Amsterdam, 1992.

[37] D. Broek, *Elementary Engineering Fracture Mechanics*, Springer Science & Business Media, 2012.

[38] Z. P. Bažant and J. Planas, *Fracture and Size Effect in Concrete and Other Quasibrittle Materials*, CRC Press, 1998.

[39] X. Yang, G. Q. Zhang, X. F. Du et al., "Measurement and implications of the dynamic fracture width in hydraulic fracturing using FBG strain sensors," in *51st U.S. Rock Mechanics/Geomechanics Symposium*, American Rock Mechanics Association, San Francisco, 2017.